

Article

High-Performance of Electrocatalytic CO₂ Reduction on Defective Graphene-Supported Cu₄S₂ Cluster

Qiyan Zhang, Yawei Li, Haiyan Zhu * and Bingbing Suo *

Shaanxi Key Laboratory for Theoretical Physics Frontiers, Institute of Modern Physics, Northwest University, Xi'an 710127, China; zhangqiyan@stumail.nwu.edu.cn (Q.Z.); yawei.li@epfl.ch (Y.L.)

* Correspondence: zhuhaiyan@nwu.edu.cn (H.Z.); bsuo@nwu.edu.cn (B.S.)

Abstract: Electrochemical CO₂ reduction reaction (CO₂RR) to high-value chemicals is one of the most splendid approaches to mitigating environmental threats and energy shortage. In this study, the catalytic performance of CO₂RR on defective graphene-supported Cu₄S₂ clusters as well as isolated Cu₄X_n (X = O, S, Se; n = 2, 4) was systematically investigated based on density functional theory (DFT) computations. Calculation results revealed that the most thermodynamically feasible product is CH₃OH among the C1 products on Cu₄X₂ clusters, in which the Cu₄S₂ cluster has the best activity concerning CH₃OH synthesis with a limiting potential of −0.48 V. When the Cu₄S₂ cluster was further supported on defective graphene, the strong interaction between cluster and substrate could greatly improve the performance via tuning the electronic structure and improving the stability of the Cu₄S₂ cluster. The calculated free energy diagram indicated that it is also more energetically preferable for CH₃OH production with a low limiting potential of −0.35 V. Besides, the defective graphene support has a significant ability to suppress the competing reactions, such as the hydrogen evolution reaction (HER) and CO and HCOOH production. Geometric structures, limiting potentials, and reduction pathways were also discussed to gain insight into the reaction mechanism and to find the minimum-energy pathway for C1 products. We hope this work will provide theoretical reference for designing and developing advanced supported Cu-based electrocatalysts for CO₂ reduction.

Keywords: electrochemical CO₂ reduction reaction; DFT calculation; Cu₄X₂ nanocluster; defective graphene-supported



Citation: Zhang, Q.; Li, Y.; Zhu, H.; Suo, B. High-Performance of Electrocatalytic CO₂ Reduction on Defective Graphene-Supported Cu₄S₂ Cluster. *Catalysts* **2022**, *12*, 454. <https://doi.org/10.3390/catal12050454>

Academic Editors: Shangqian Zhu, Qinglan Zhao and Yao Yao

Received: 16 March 2022

Accepted: 14 April 2022

Published: 19 April 2022

Publisher's Note: MDPI stays neutral with regard to jurisdictional claims in published maps and institutional affiliations.



Copyright: © 2022 by the authors. Licensee MDPI, Basel, Switzerland. This article is an open access article distributed under the terms and conditions of the Creative Commons Attribution (CC BY) license (<https://creativecommons.org/licenses/by/4.0/>).

1. Introduction

Global warming and energy shortage have become two major issues in the 21st century. The excessive CO₂ emission caused by rapid consumption of fossil resources calls for the instant requirement of clean and renewable energy [1]. CO₂ itself is an inert molecule ($\Delta G_f^0 = -394.4$ KJ/mol) [2], so it is urgent to explore a robust catalyst for its reduction and conversion. In recent years, electrochemical CO₂ reduction reaction (CO₂RR) has attracted widespread attention as one of the most excellent methods to alleviate energy shortage and reduce the global carbon footprint [3,4]. In CO₂RR, various metal electrodes play a dual role, not only as an electron conducting medium but also as catalytically active sites. Among them, Cu-based material has excellent activity and selectivity to reduce CO₂ into hydrocarbons such as methanol, methane, formic acid, ethylene, etc. [5,6]. In these products, methanol is a desired hydrocarbon because it can be used as feedstock for direct methanol fuel cells [7]. More importantly, the metallic Cu has been verified as an active catalyst for methanol synthesis with a turnover frequency even comparable with that of industrial catalysts [8].

With the development from single-crystal metal electrodes to supported metal nanoparticle electrodes [9–11], the supported sub-nanometric Cu clusters [12,13] have received considerable attention in the past few years. The superior catalytic performance comes from three factors: The unique electronic structure of the nano-size cluster; the high specific

surface area; and the significant effect of the substrate support. In the catalytic experiments, the support has an important role in immobilizing clusters and preventing them from aggregation. For instance, defect engineering of graphene [14,15] has been used to immobilize the cluster against sinter by providing strong anchoring sites which could effectively regulate the electronic properties and catalytic performance in CO₂ reduction. In particular, theoretical results have confirmed that the defective graphene supported Cu (Cu₅₅ [16] and Cu₄ [17]) nanocluster can improve the CO₂RR selectivity for hydrocarbon fuels at low overpotential. Additionally, Ma et al. reported that the experimental realization of the Cu@Cu_xO nanoparticles decorated on defective graphene achieved a high CO₂ reduction Faradaic efficiency of 60.6% [18]. By analyzing experiments and DFT calculations, Hu et al. demonstrated that the defective graphene-supported Cu₁₃ cluster exhibits excellent performance for CO₂RR with a maximum Faradaic efficiency towards methane of 81.7% and an outstanding stability of 40 h [19].

It is noteworthy that the activity and selectivity of CO₂RR are highly sensitive to the structure of the supported Cu-based cluster [20]. To date, the size-selected Cu₄ cluster is found to present good catalytic activity for producing hydrocarbons at near atmospheric pressure by comparing with other larger-size catalysts [21,22]. In the experiment, the subnanometer-sized Cu nanoclusters have been successfully prepared. For example, the size-controlled naked Cu cluster [23–25] can be synthesized by the electrochemical oxidation-reduction method and the one-pot procedure based on wet chemical reduction, or combination of gas-phase cluster ion sources, mass spectrometry, and soft-landing techniques. However, the impurity-doping effects could further enhance the durability, selectivity, and chemical activity of clusters. The modified Cu nanoclusters [26,27] in the experiment and the theoretical have attracted extensive attention with the development of experimental synthetic techniques. For example, Uzunova et al. found that the Cu₃₂O₁₆ and Cu₁₄O₇ nanoclusters can improve the catalytic performance of CO₂RR to hydrocarbons because of their strong interaction with CO₂ [28]. Similarly, Zhao et al. reported that the CuS nanosheet arrays supported on nickel foam are a robust catalyst for CO₂RR toward methane, which has high Faradaic efficiency of 73 ± 5% and a low Tafel slope of 57 mV dec⁻¹ [29]. Lu et al. have synthesized Cu₃-X clusters (Cu₃-Cl, Cu₃-Br, Cu₃-NO₃) which have high selectivity for the electrocatalytic reduction of CO₂ to C₂H₄ with a maximum Faradaic efficiency of 55.01% [30].

It can be seen that control type, location, and content of the dopant atoms are important in terms of affecting the catalytic performance for the modified cluster [31,32]. The electronic structure of the nanocluster can be easily regulated by per-oxidation or heteroatom modulation, providing remarkable possibilities to tune the catalytic performance in CO₂RR. What is the effect of doped clusters on the catalytic activity and selectivity of CO₂ reduction with different valence states Cu as electrocatalyst? How does the defective graphene support affect their performance? To answer these questions, high-precision computational methods are first used to give an in-depth understanding of the CO₂ reduction mechanism of the isolated Cu₄X_n clusters, to identify the promising candidate with optimal catalytic performance. On this basis, the CO₂RR mechanism of the Cu₄S₂ cluster adsorbed on defective graphene is considered as a representative model to boost its stability and application. The catalytic activity and product selectivity are evaluated via analyzing the limiting potential of CO₂RR towards different C1 products. The geometric structure, charge distribution, and all possible reaction pathways were also discussed to help further understand the reaction mechanism and catalytic properties. We also hope that this work can give theoretical guidance for experimental research and provide reference for the design of high-performance supported Cu-based catalysts in the future.

2. Results and Discussion

2.1. Mechanism of CO₂RR on the Cu₄X₂ Cluster

2.1.1. Cu₄X₂ Cluster and Electrochemical Adsorption of CO₂

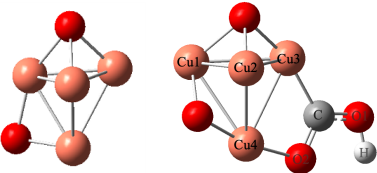
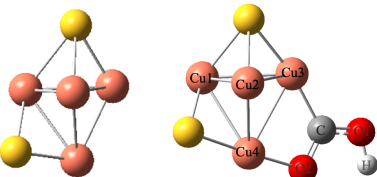
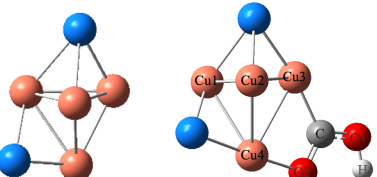
Potential energy surfaces (PESs) of the Cu₄X₂ clusters were probed via global optimization algorithms to locate the global minima (GM) structure and low-lying energy isomers (details in Figure S1). The GM of the Cu₄O₂, Cu₄S₂, Cu₄Se₂ cluster exhibit a similar configuration (in Table 1), in which four Cu atoms and one doped atom form a double trigonal pyramidal structure, and the other doped atom binds with two Cu atoms on the side edge of Cu₄. With the decrease of electronegativity of the doped atom, the Cu₄X₂ configuration exhibits small stretch in the xy plane; as for the vertical direction, the lower half (triangular pyramid of Cu₄ structure) presents a slight compression, while the upper half presents a small stretch. It is noteworthy that the structure of the Cu₄S₂ cluster predicted in this paper is partly consistent with the lowest energy structure of the Cu_nS (n = 4) cluster proposed by Li et al. [33], verifying the solidity of our results. The natural bond orbital (NBO) analysis presented in Table S2 shows that the higher electronegativity dopant atoms can form the positively charged Cu sites, which tends to attract the electronegative oxygen in CO₂, thus facilitating the initial step of CO₂RR.

It is easy to understand that the ability of capturing CO₂ molecules is essential as the introductory step in CO₂RR. The electrochemical adsorption of CO₂ molecules can be typically represented as



The electrochemical adsorption of CO₂ involves one (H⁺ + e⁻) pair transfer to the CO₂ species, where CO₂ is first hydrogenated to generate hydroxyl or carboxyl groups; it is usually controlled via an applied potential. After testing the possible electrochemical adsorption sites of CO₂, the calculated reaction free energy of COOH* formation is 0.41 eV, 1.02 eV, and 0.73 eV lower than that of OCHO* formation on the Cu₄O₂, Cu₄S₂, Cu₄Se₂ clusters, respectively. This means that the intermediate COOH* is more preferable in this case, and the lowest-energy configuration is located and presented in Table 1. As seen in Table 1, all reaction free energies are negative, indicating that the electrochemical absorption of CO₂ can occur spontaneously. In these three clusters, E_{react} of COOH* on Cu₄S₂ and Cu₄Se₂ are close, but still larger than that of Cu₄O₂, suggesting the former two clusters are more active for CO₂ activation. In the adsorbate COOH, both C and O are binding with the Cu atoms. The binding distances $d_{(\text{Cu}-\text{C})}$ and $d_{(\text{Cu}-\text{O})}$ enlarge slightly with the decrease of electronegativity of the chalcogen; that is in line with the trend of charge transfer between cluster and adsorbed species. The charge redistributions before and after electrochemical CO₂ adsorption are listed in Table S3. The NBO analysis revealed that the adsorption process is accompanied with partial charge transfer of about -0.5 from the Cu₄X₂ cluster (electron donor) to the COOH adsorbate (electron acceptor). Meanwhile, the transferred charge decreases from Cu₄O₂ to Cu₄S₂ (or Cu₄Se₂), resulting in the weakness of Cu-O and Cu-C bonding between COOH* and Cu₄S₂ (or Cu₄Se₂). In addition, the structures of COOH* on three different clusters are similar, in which $\angle_{\text{O}-\text{C}-\text{O}}$ bends significantly compared with the linear CO₂ molecule. Besides, both C-O bonds are elongated to ensure that COOH* retains sufficient activity to continue the subsequent hydrogenation reactions. Notice that the adsorption of COOH* does not change the main structure of doped clusters, which is important to maintain the stability of the Cu₄X₂ cluster in the CO₂RR process.

Table 1. The GM of the Cu_4X_2 cluster and structural details of electrochemical CO_2 adsorption on the Cu_4X_2 cluster.

Cluster	Electrochemical Adsorption of CO_2			
	COOH^*	E_{react}	δ^+	Geometric Parameters
		−0.24	0.55	$d_{(\text{Cu}_3-\text{C})}$
				1.91
				$d_{(\text{Cu}_4-\text{O})}$
				1.89
$d_{(\text{C}-\text{O}_1)}$	$d_{(\text{C}-\text{O}_2)}$			
1.33	1.26			
$d_{(\text{O}_1-\text{H})}$	$\angle_{\text{O}-\text{C}-\text{O}}$			
0.98	114.9			
		−0.65	0.52	$d_{(\text{Cu}_3-\text{C})}$
				1.92
				$d_{(\text{Cu}_4-\text{O})}$
				1.90
$d_{(\text{C}-\text{O}_1)}$	$d_{(\text{C}-\text{O}_2)}$			
1.33	1.26			
$d_{(\text{O}_1-\text{H})}$	$\angle_{\text{O}-\text{C}-\text{O}}$			
0.98	115.3			
		−0.57	0.52	$d_{(\text{Cu}_3-\text{C})}$
				1.93
				$d_{(\text{Cu}_4-\text{O})}$
				1.91
$d_{(\text{C}-\text{O}_1)}$	$d_{(\text{C}-\text{O}_2)}$			
1.33	1.27			
$d_{(\text{O}_1-\text{H})}$	$\angle_{\text{O}-\text{C}-\text{O}}$			
0.98	115.2			

The red, yellow, blue, orange, gray, and white spheres denote O, S, Se, Cu, C, and H atoms, respectively. The unit for E_{react} is eV, d is Å, and $\angle_{\text{O}-\text{C}-\text{O}}$ is $^\circ$.

2.1.2. Reaction Pathway of CO_2RR on the Cu_4X_2 Cluster

In order to obtain a better understanding of the reaction mechanism of electrocatalytic CO_2 reduction, the reaction networks for each elementary step were analyzed to identify the most thermodynamically favorable pathway and major side reactions of each doped cluster. The reaction schemes of all possible pathways for the reduction of CO_2 to methanol or methane, as well as their competing reactions, are given in the Supplementary Materials. The lowest energy pathway of CO_2RR to CH_3OH and CH_4 is shown in Figure 1, which helps us to explore the catalytic performance explicitly.

As shown in Figure 1, the free energy diagram of CO_2RR pathways on the Cu_4X_2 clusters starts from the intermediate COOH^* . The lowest energy pathway for CH_3OH formation is identified (pathway 1, in blue), and the other pathway (pathway 2, in red) represents CO_2RR towards CH_4 formation. The electrochemical adsorption of CO_2 on the Cu_4O_2 , Cu_4S_2 , and Cu_4Se_2 clusters are accompanied with a spontaneous exothermic process with ΔG of -0.24 eV, -0.65 eV, and -0.57 eV, respectively, which means the initial step can effectively adsorb COOH^* (state 1). Subsequently, the hydroxyl group is hydrogenated on C to form HCOOH^* accompanied by a Cu-C bond cleavage or a Cu-O bond cleavage caused by hydrogenation on O; these are both endothermic reactions, while the ΔG of the former is 0.58 eV, 0.50 eV, and 0.12 eV lower than the latter on the Cu_4O_2 , Cu_4S_2 , and Cu_4Se_2 clusters, respectively. Then, the intermediate HCOOH^* (state 2) undergoes three degrees of hydrogenation to generate CHO^* (state 3), CH_2O^* (state 4), and CH_3O^* (state 5). Finally, the adsorbate CH_3O is hydrogenated at the oxygen atom to produce CH_3OH . The rate-determining steps of pathway 1 on the Cu_4O_2 and Cu_4S_2

cluster are both the hydrogenation of COOH^* to form HCOOH^* (from 1 \rightarrow 2), which is endergonic, and require potentials of -0.56 V and -0.48 V, respectively. However, the rate-determining step for the Cu_4Se_2 cluster is created concerning CHO^* (from 2 \rightarrow 3) via a $(\text{H}^+ + \text{e}^-)$ pair transfer from a solution with a larger potential of -0.82 V. It is obvious that the Cu_4S_2 cluster has the minimum rate limiting reaction energy in methanol formation among these clusters, indicating that it can be considered as a promising electrocatalyst for CH_3OH formation during the CO_2 reduction process.

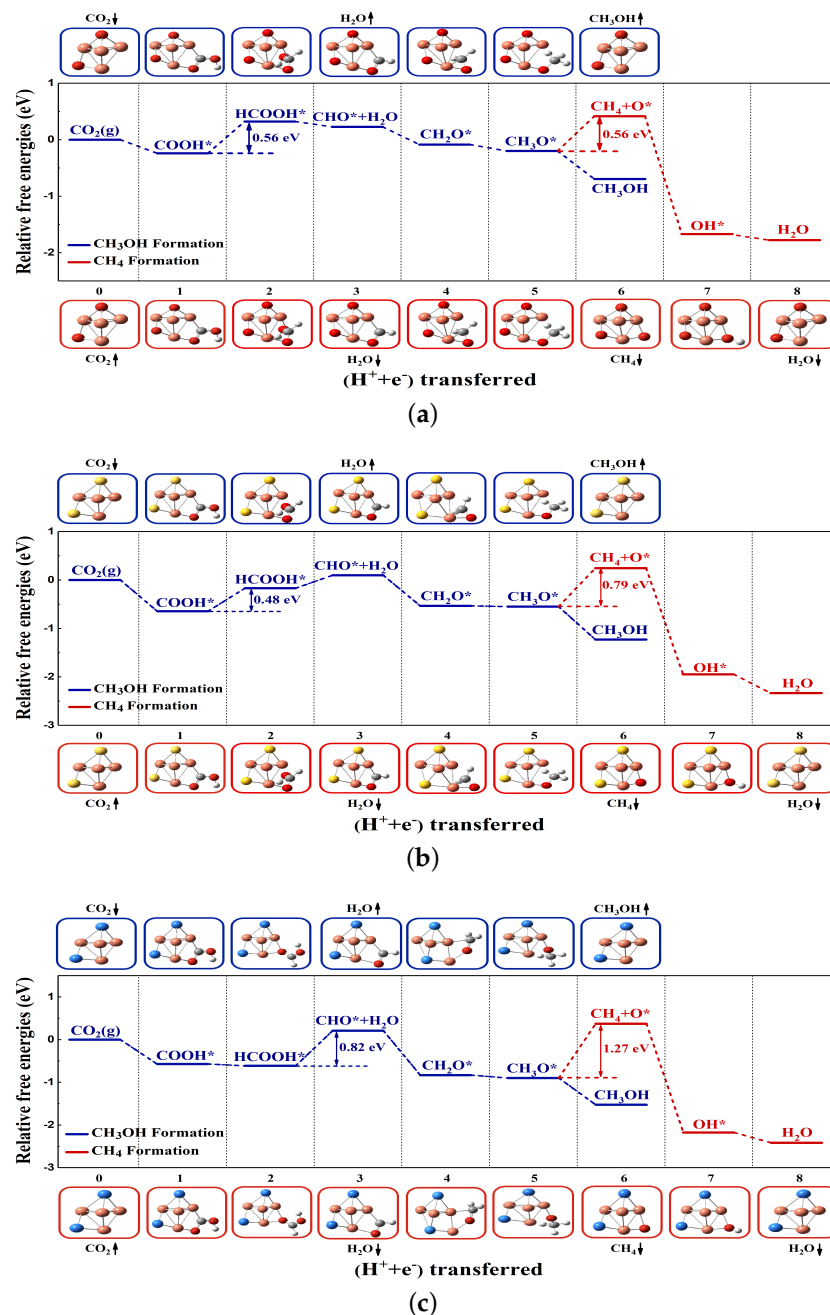


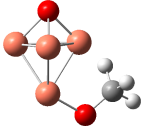
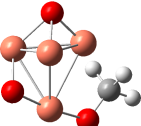
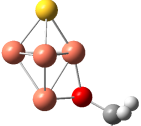
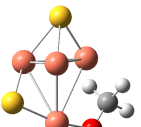
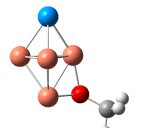
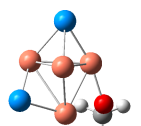
Figure 1. The lowest free energy diagram of CO_2RR to CH_3OH and CH_4 with no applied potential on Cu_4O_2 (a), Cu_4S_2 (b), and Cu_4Se_2 (c) clusters. (The blue line represents the methanol formation pathway, with the intermediate products shown in the upper part of the figure. The red line represents the methane formation pathway, with the intermediate products shown in the lower part of the figure).

In pathway 2 for methane formation, the COOH^* undergoes a series of hydrogenations and takes the form of $\text{COOH}^* \rightarrow \text{HCOOH}^* \rightarrow \text{CHO}^* \rightarrow \text{CH}_2\text{O}^* \rightarrow \text{CH}_3\text{O}^* \rightarrow \text{CH}_4 + \text{O}^* \rightarrow \text{OH}^* \rightarrow \text{H}_2\text{O}$. At this point, desorption of CH_4 is the most difficult step in pathway 2 with limiting potentials of -0.56 V, -0.79 V, and -1.27 V for the Cu_4O_2 , Cu_4S_2 , and Cu_4Se_2 clusters, respectively. A free energy profile shows that there are partially overlapping intermediates between pathways 1 and 2, while the sixth step is the product-determining step for producing methanol or methane. The kinetic barrier diagram of the sixth step on the Cu_4O_2 cluster, the Cu_4S_2 cluster, and the Cu_4Se_2 cluster is shown in Figure S5. The corresponding results show that the energy barrier for CH_3OH formation is 1.73 eV, 0.99 eV, and 1.49 eV lower than that of CH_4 formation, respectively. Combined with the free energy diagram, the methanol production step is a spontaneous exothermic process, while the release of methane is endothermic, suggesting the methanol product is both thermodynamically and kinetically favored on the Cu_4X_2 clusters.

2.1.3. The Catalytic Performance on Cu_4X_2 Cluster

The activity of the CO_2 -to- CH_3OH reaction is governed by the limiting potentials, which are -0.56 V, -0.48 V, and -0.82 V for the Cu_4O_2 , Cu_4S_2 , and Cu_4Se_2 clusters, respectively. The results indicated that both the Cu_4O_2 and Cu_4S_2 clusters exhibit excellent electrocatalytic activity for methanol synthesis. The presence of two heteroatoms can tune the electronic structure of the adjacent Cu atom, leading to partial charge transfer from Cu to chalcogen. Therefore, the oxidized Cu^+ site can effectively promote CO_2 activation, which is an important intermediate for triggering an electroreduction reaction. For the selectivity of the Cu_4X_2 cluster, the CH_3OH formation step is a spontaneous exothermic process, while the branch of CH_4 production requires an endothermic process to proceed, in which the intermediate CH_3O^* is considered as a bifurcation for these two pathways. Therefore, the Cu_4X_2 cluster exhibits high CO_2 selectivity for CH_3OH synthesis, instead of producing CH_4 via $\text{CHO}^* \rightarrow \text{CH}_2\text{O}^* \rightarrow \text{CH}_3\text{O}^* \rightarrow \text{CH}_4$ on the Cu_4X cluster [34]. In order to analyze the variation of product selectivity with dopant content, we then examine the bond length, bond energy, and adsorption energy of the adsorbate CH_3O on Cu_4X_2 and Cu_4X clusters. As shown in Table 2, the CH_3O^* binds to the cluster via an oxygen atom; product selectivity at this point depends on how easily the Cu-O or C-O bond can be cleaved. With the dopant content increasing, the bond energy of Cu-O becomes smaller and that of C-O becomes larger, which is consistent with the changes in bond length. The adsorption energy of CH_3O^* on the Cu_4X_2 cluster is smaller than that on the Cu_4X cluster, which implies the subsequent reaction prefers the desorption of methanol on the Cu_4X_2 cluster. These calculations further confirmed that the production of CH_3OH is more favorable than that of CH_4 on the Cu_4X_2 cluster. In addition, the doping of four O, S, and Se atoms on the Cu_4 cluster has also been tested as an electrocatalyst in CO_2RR for comparison. The activity of the Cu_4X_4 cluster will not be explained in detail as it is not improved, and the discussion can be found in the Supplementary Material.

Table 2. The structural details and adsorption energy of intermediate CH_3O^* on Cu_4X and Cu_4X_2 ($\text{X}=\text{O}, \text{S}, \text{Se}$) cluster.

Cluster	CH_3O^*	Bond Length		Bond Energy		Adsorption Energy
		$d_{(\text{Cu}-\text{O})}$	$d_{(\text{C}-\text{O})}$	$E_{(\text{Cu}-\text{O})}$	$E_{(\text{C}-\text{O})}$	
Cu_4O		1.83	1.38	53.93	95.46	−1.59
Cu_4O_2		1.85	1.37	48.04	101.90	−0.57
Cu_4S		1.89	1.41	55.35	78.30	−1.53
Cu_4S_2		1.84	1.37	41.71	96.76	−0.33
Cu_4Se		1.89	1.41	53.98	77.23	−2.01
Cu_4Se_2		1.87	1.41	49.44	98.31	−0.65

The red, yellow, blue, orange, gray, and white spheres denote O, S, Se, Cu, C, and H atoms, respectively. The unit for bond length, bond energy, and adsorption energy is Å, KJ/mol, and eV, respectively.

2.2. CO_2RR Pathway on the Defective Graphene Supported Cu_4S_2 Cluster

2.2.1. Geometric Structure and Stability of the Catalyst Model

In view of above discussions, the Cu_4S_2 cluster is found to be an excellent catalyst due to its being more favorable for CH_3OH production and having low limiting potential in CO_2RR . Based on the clear understanding of the reduction mechanism of doped clusters, we are committed to investigating the defective graphene supported Cu_4S_2 cluster as a promising electrode material for CO_2RR , so as to broaden its practical applications. The geometric structure and stability of the Cu_4S_2 cluster which is adsorbed on defective graphene in different orientations are first tested in the case of the fully relaxed system. Figure 2 shows the optimized structure and the charge distributions with the lowest-energy binding configuration (denoted as $\text{Cu}_4\text{S}_2/\text{SV}$). The removal of one carbon atom from the graphene sheet leads to the undercoordination of three C atoms around the vacancy, which exerts strong attraction for the Cu atom and allows the Cu_4S_2 cluster to be stably anchored to the defective graphene. From Figure 2a, the Cu atom at the bottom forms three covalent bonds with the adjacent C atoms on the defective graphene, and the average height of the cluster from the defective surface is 1.61 Å. The electrons of the Cu_4S_2 cluster prefer to transfer to the substrate, resulting in the positive charges on the cluster with the value of 3.89 e. The density of states (in Figure S7) reveals the metallic behavior that makes

the structure unique and have good conductivity, and the C and Cu form a new bond corresponding to the overlap of the C *p* and Cu *d* orbitals. Moreover, the binding energy of anchoring the Cu₄S₂ cluster at the single vacancy site of graphene (V_C) is to be defined as:

$$E_b = E_{V_C} + E_{cluster} - E_{total}, \quad (3)$$

where the E_{total} , E_{V_C} , and $E_{cluster}$ represent the total energy of the Cu₄S₂/SV system, the graphene with a single vacancy, and the Cu₄S₂ cluster, respectively. From the calculation result, the binding energy of the Cu₄S₂/SV system is +5.07 eV, indicating that the supported Cu₄S₂ cluster can be stably located on the defective graphene and continue the follow-up reactions.

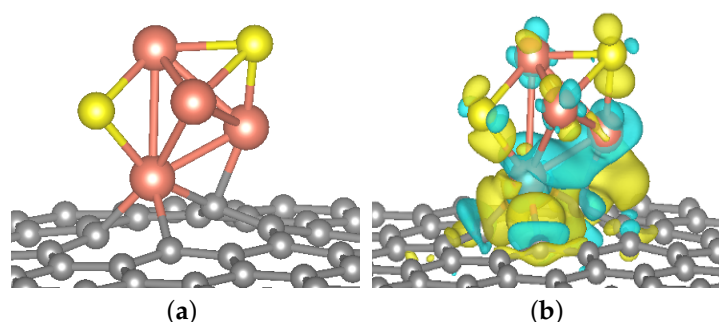


Figure 2. The optimized structure (a) and charge density difference plot (b) for the Cu₄S₂/SV catalyst. The yellow and blue color regions mean the charge accumulation and depletion, respectively.

2.2.2. Reaction Pathway of CO₂RR on Cu₄S₂/SV

As the initial step of Cu₄S₂/SV in CO₂RR, the first hydrogenation reaction involves a (H⁺ + e⁻) pair transfer to CO₂. There are two possible adsorbed species, COOH* or OCHO*, in competition with the H* for HER, as illustrated by Equations (1), (2), and (4), respectively.



In both cases of CO₂ activation, the linear structure of the CO₂ molecule transfers into a bent structure for further CO₂RR. The calculated reaction free energy of the CO₂ hydrogenation occurs on the O site to form intermediate COOH* (0.24 eV) and is found lower than that on C to form OCHO* (0.40 eV). To examine the selectivity of HER on CO₂RR, as shown in Figure 3a, the reaction free energy for H* formation is 0.58 eV larger than that of COOH* formation. This means that the Cu₄S₂/SV catalyst displays higher CO₂RR activity as well as lower HER activity. Thus, the CO₂ reduction occurs predominantly before the HER process.

In this part, the reaction mechanism for electroreduction of CO₂ to CH₃OH, CH₄, HCOOH, and CO was investigated, beginning with the intermediate COOH*. Among these, the formations of CO and HCOOH are accompanied by the two transfer steps of (H⁺ + e⁻) pairs, and the reaction pathways are presented in Figure 3b and 3c, respectively. For the Cu₄S₂/SV catalyst, the optimum pathway of CO production goes through the pathway CO₂ → COOH* → CO* → CO. The rate-determining step is the hydrogenation of the hydroxyl group to generate the CO*, whose limiting potential is calculated to be -1.43 V. In the process of HCOOH generation, the last step of HCOOH desorption is the rate-determining step with a high free energy change of 1.15 eV. This is due to the stable adsorption of HCOOH* that hinders its desorption from the catalyst surface. The results clearly showed that these high limiting potentials exhibit poor selectivity for producing CO and HCOOH. In addition, the basic steps of all possible intermediates of CO₂ hydrogenation to C1 products on the Cu₄S₂/SV catalyst and their corresponding reaction free energies are shown in Figure 3d. There are several thermodynamically feasible pathways for the

reduction of CO₂ to CH₃OH and CH₄, in which the lowest free energy diagrams are listed in Figure 4.

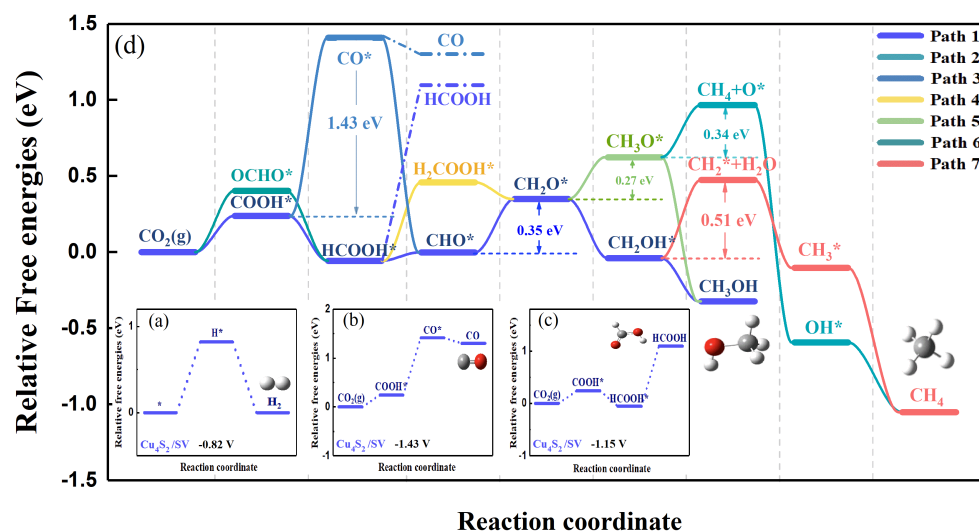


Figure 3. Reaction pathways to produce H₂ (a), CO (b), and HCOOH (c) on the Cu₄S₂/SV catalyst with no applied potential. The potential required to carry out over the most endergonic step is listed in the legend. The mechanistic free energy diagram of CO₂RR on the Cu₄S₂/SV catalyst with no applied potential (d). The colorful solid lines label thermodynamically feasible reaction pathways, in which each step involves a (H⁺ + e[−]) pair transfer. The step of CO or HCOOH desorption (in dashed line) is a thermochemical process that does not involve (H⁺ + e[−]) pair transfer.

The blue line in Figure 4 shows the lowest energy reaction pathway for producing CH₃OH accompanied by six (H⁺ + e[−]) pair transfer processes. The first hydrogenation favors the formation of COOH* (state 1); the next step is to generate an adsorbed HCOOH* (2) through transfer of another (H⁺ + e[−]) pair. Subsequently, HCOOH* is successively hydrogenated to produce CHO* (3) and CH₂O* (4). Notably, the fifth step of the proton and electron transfer leads to generation of CH₂OH* (5), where the free energy of the evolution of CH₂OH* is 0.66 eV lower than the formation of CH₃O*. Finally, the CH₂OH* can be hydrogenated to form CH₃OH (6). In the pathway of CH₃OH formation, the rate-determining step is CHO* → CH₂O* with a low limiting potential of −0.35 V. The great activity is caused by the strong interaction between Cu₄S₂ and defective graphene, which could further tune the electronic structure and stability of the supported cluster. The charge transfer from the cluster to the substrate indicates the Cu *d* orbitals become more vacant and available to be adsorbates. Another red line represents the pathway which takes eight (H⁺ + e[−]) pairs of transfer steps to produce methane. In Figure 4, the pathway to generate methanol and methane diverges in the sixth step: one is a pair proton–electron transfer to the C end of CH₂OH* and eventually produces methanol; the other is to form the H₂O molecule first, and then the remaining CH₂* undergoes continuous hydrogenations to produce methane at last. Obviously, the step of CH₃OH formation is thermodynamically downhill, rather than the branch of CH₄ formation requiring the endothermic sort for the next hydrogenation reaction. Hence, the Cu₄S₂/SV electrode material is more energetically preferable for CH₃OH production compared with other C1 products in CO₂ reduction. For the pathway of CH₄ formation, the calculation shows that removing the OH* from the catalyst is the most endothermic step during the whole reaction process. In this case, the step of releasing H₂O becomes the rate-determining step, of which the limiting potential is −0.51 V. Due to the limiting potential of CH₃OH formation being lower than that of CH₄ formation, the former may be preferred from a thermodynamic point of view.

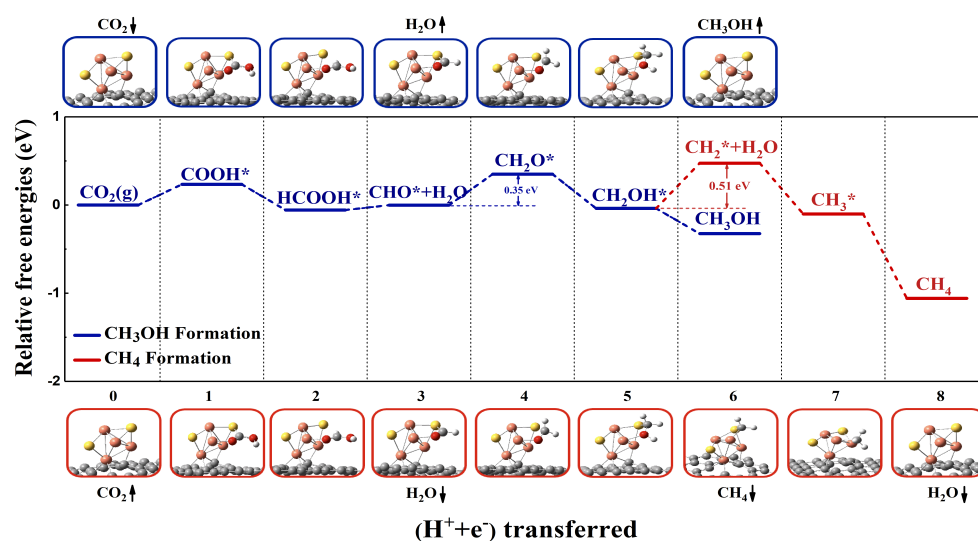


Figure 4. Reaction pathways for producing CH₃OH and CH₄ on the Cu₄S₂/SV catalyst with no applied potential. (The blue line represents the methanol formation pathway which the intermediate products show in the upper part of the figure. The red line represents the methane formation pathway which the intermediate products show in the lower part of the figure).

Based on the above discussions, the calculation results indicate that the Cu₄S₂/SV catalyst is not only more favorable for generating CH₃OH but also can effectively suppress the competing reactions, such as HER, CO, and HCOOH production. In addition, recent experiments [35–37] have shown that the supported Cu-based electrode as a electrocatalyst for CO₂RR has higher CH₃OH selectivity, suggesting that the free energy changes for generating CH₃OH are smaller than those of other products. This is consistent with our calculation.

3. Computational Details

Density functional theory (DFT) [38] calculations were used to investigate the reaction mechanism of isolated Cu₄X_n clusters in CO₂ reduction. The first section in this study is to search for local or even global minima of molecular clusters using ABCluster software [39] which adopts an artificial bee colony algorithm to conduct the global optimization and conformation search. Full details about the global minima nanocluster searching process are available in the Supplementary Material. After that, the subsequent geometry optimizations and vibration frequencies were implemented at the level of B3LYP/6–31g(d, p) [40,41] by the Gaussian16 program [42]. Next, the various active sites for electrochemical CO₂ adsorption and hydrogenation reactions on the doped clusters were tested. Following that, the electronic energies were refined with the single-point energy calculation employing the high-level DLPNO-CCSD(T) method [43], along with the cc-pVTZ basis set [44] using the ORCA software [45]. The Gibbs free energies were then obtained through electronic energies at the DLPNO-CCSD(T)/cc-pVTZ level of theory corrected with the zero-point energies (ZPEs) computed by the B3LYP/6–31g(d, p) method. Besides, the conductor-like polarizable continuum model (CPCM) [46] with toluene as the solvent was used in this study. Finally, the reasonable intermediates were sieved using the calculation mentioned above, after that we could obtain the most feasible pathway for CO₂ reduction for different products on the doped clusters.

The calculations about the defective graphene supported doped cluster were conducted using the Vienna ab initio simulation package (VASP, version 5.3.2) [47], which is based on the DFT with the projector-augmented wave method (PAW) [48]. The PBE exchange-correlation functional [49] and van der Waals (vdW) interactions described via a pair-wise force field by the DFT-D2 method of Grimme [50] were adopted for all the defective graphene-supported system calculations. In this work, the model structure comprises

5 × 5 single-layer graphene unit cells with a single vacancy as the substrate, and the doped cluster was placed above the vacancy site. The vacuum region was set as 15 Å for preventing the mirror images effect. The Monkhorst–Pack mesh k -points 4 × 4 × 1 was used for calculation, and a plane-wave energy cutoff is used of 520 eV after convergence test (see Figure S8). All the atoms were allowed to relax during the model optimization process. The total energy converged to 10^{−7} eV and the maximum ionic force was less than 0.01 eV/Å. In addition, VASPsol [51] was used to describe the effect of electrostatics, cavitation, and dispersion on interactions between solutes and solvents. The VASPsol model considering the solvent molecule as the continuum solvent, and the dielectric constant were used to represent the solvent effect. Here, the dielectric constant of toluene $\epsilon = 2.37$ was used to simulate the implicit solvent environment.

The computational hydrogen electrode (CHE) model was described by Nørskov et al. in 2004 [52], and is combined with energetic from DFT simulations to calculate the free energy changes (ΔG) for various basic steps of CO₂ reduction. In the CHE model, the chemical potential of a proton–electron pair is defined as half of the gaseous H₂ at equilibrium, under any pH values and temperatures, the reaction



is equilibrated at 0 V, 1325 Pa reversible hydrogen electrode (RHE). The free energy for a basic electrochemical reduction step is defined as



Here, “*” denotes an active site on the catalyst. Then the potential-dependent free energy change is thus defined as

$$\Delta G = \mu(\text{AH}^*) - \mu(\text{A}^*) - [1/2\mu(\text{H}_2) - eU]. \quad (7)$$

in which μ is the chemical potential, e is the elementary positive charge and U is the electrode potential versus RHE. The chemical potential is shifted by $-eU$ when an external potential U is applied. While at zero applied potential, ΔG becomes $-U_L/e$, in which U_L means the limiting potential in the CO₂RR process.

4. Conclusions

To sum up, the reaction mechanism of CO₂ electroreduction to C1 products on a defective graphene-supported Cu₄S₂ cluster and isolated Cu₄X_n clusters was investigated. DFT calculations indicated the CH₃OH is the most feasible product among the C1 products on Cu₄X₂ clusters, and the limiting potentials for producing CH₃OH are in the order of Cu₄S₂ < Cu₄O₂ < Cu₄Se₂. The Cu₄S₂ cluster has excellent selectivity and the best catalytic activity (−0.48 V) during the conversion of CO₂ to CH₃OH among these isolated clusters. For the Cu₄S₂/SV catalyst, defect-engineered graphene could induce a strong interaction between cluster and substrate, which facilitates the improved catalytic performance through adjusting the electronic structure and stability of the Cu₄S₂ cluster. The Cu₄S₂/SV catalyst not only shows superior activity to produce CH₃OH with a low potential of −0.35 V, but can also significantly suppress other competing reactions, such as HER, CO and HCOOH production. We hope the combination of modification effect and defective support engineering can provide a valuable strategy for the Cu-based catalyst design with highly electrocatalytic performance in CO₂ reduction.

References [53–57] are cited in the Supplementary Materials.

Supplementary Materials: The following supporting information can be downloaded at: <https://www.mdpi.com/article/10.3390/catal12050454/s1>, Figure S1: The ground minimal structures and low-lying energy isomers of the gas-phase Cu₄X₂ clusters. Figure S2: Global minimum geometry composition and some selected bond lengths of Cu₄X₂ clusters and Cu₄X₄ clusters; Figure S3:

Mechanistic free energies diagram of electrochemical CO₂ reduction on Cu₄O₂ cluster, Cu₄S₂ cluster, and Cu₄Se₂ cluster with no applied potential; Figure S4: Free energies diagram for producing H₂, CO, and HCOOH with no applied potential; Figure S5: Kinetic barrier diagram of product-determining step on Cu₄O₂ cluster, Cu₄S₂ cluster, and Cu₄Se₂ cluster; Figure S6: Mechanistic free energies diagram of electrochemical CO₂ reduction on the Cu₄O₄ cluster, Cu₄S₄ cluster, and Cu₄Se₄ cluster with no applied potential; Figure S7: Total density of states (DOS) of Cu₄S₂/SV catalyst, Projected density of states (PDOS) of *p* orbitals of C, and PDOS of *d* orbitals of Cu; Figure S8: Variation the reaction free energy of COOH* on Cu₄S₂/SV catalyst as a function of the cutoff energy value in the plane-wave calculations; Table S1: Geometric parameters, the maximum, and minimum harmonic vibrational frequencies of the GM structure of gas-phase Cu₄X₂ clusters; Table S2: The charge distribution of elements in the neutral Cu₄X, Cu₄X₂, and Cu₄X₄ clusters by the natural bond orbital charge analysis; Table S3: The charge distribution of elements in the neutral Cu₄X, Cu₄X₂, and Cu₄X₄ clusters with electrochemical CO₂ adsorption by the natural bond orbital charge analysis.

Author Contributions: Data curation, Q.Z.; Investigation, Q.Z., Y.L. and H.Z.; Writing—original draft, Q.Z.; Writing—review and editing, Q.Z., H.Z. and B.S. All authors have read and agreed to the published version of the manuscript.

Funding: This research was funded by the National Natural Science Foundation of China (21803041, 51572219, and 21873077), the Natural Science Foundation of Shaanxi Province of China (No.2018JM1010 and 2019JM-592), the Graduate's Innovation Fund of the Northwest University of China (No. YJG15007) and the Double First-class University Construction project of Northwest University.

Institutional Review Board Statement: Not applicable.

Informed Consent Statement: Not applicable.

Data Availability Statement: The data presented in this study and not reported in the Supplementary Materials are available on request from the corresponding author.

Conflicts of Interest: The authors declare no conflict of interest.

References

1. Dinh, C.; Burdyny, T.; Kibria, M.G.; Seifitokaldani, A.; Gabardo, C.M.; De, A.; Kiani, A.; Edwards, J.P.; De Luna, P.; Bushuyev, O.S.; et al. CO₂ electroreduction to ethylene via hydroxide-mediated copper catalysis at an abrupt interface. *Science* **2018**, *360*, 783–787. [[CrossRef](#)] [[PubMed](#)]
2. Kortlever, R.; Shen, J.; Schouten, K.J.P.; Calle Vallejo, F.; Koper, M.T. Catalysts and reaction pathways for the electrochemical reduction of carbon dioxide. *J. Phys. Chem. Lett.* **2015**, *6*, 4073–4082. [[CrossRef](#)] [[PubMed](#)]
3. Wang, W.; Wang, S.; Ma, X.; Gong, J. Recent advances in catalytic hydrogenation of carbon dioxide. *Chem. Soc. Rev.* **2011**, *40*, 3703–3727. [[CrossRef](#)] [[PubMed](#)]
4. Federsel, C.; Jackstell, R.; Beller, M. State-of-the-art catalysts for hydrogenation of carbon dioxide. *Angew. Chem. Int. Ed. Engl.* **2010**, *49*, 6254–6257. [[CrossRef](#)] [[PubMed](#)]
5. Hori, Y. Electrochemical CO₂ Reduction on Metal Electrodes. In *Modern Aspects of Electrochemistry*; Springer: New York, NY, USA, 2018; Volume 42, pp. 89–189. [[CrossRef](#)]
6. Jiao, J.; Lin, R.; Liu, S.; Cheong, W.C.; Zhang, C.; Chen, Z.; Pan, Y.; Tang, J.; Wu, K.; Hung, S.F.; et al. Copper atom-pair catalyst anchored on alloy nanowires for selective and efficient electrochemical reduction of CO₂. *Nat. Chem.* **2019**, *11*, 222–228. [[CrossRef](#)]
7. Olah, G.A.; Goepfert, A.; Prakash, G.S. Chemical recycling of carbon dioxide to methanol and dimethyl ether: from greenhouse gas to renewable, environmentally carbon neutral fuels and synthetic hydrocarbons. *J. Org. Chem.* **2009**, *74*, 487–498. [[CrossRef](#)]
8. Rawat, K.S.; Mahata, A.; Pathak, B. Thermochemical and electrochemical CO₂ reduction on octahedral Cu nanocluster: Role of solvent towards product selectivity. *J. Catal.* **2017**, *349*, 118–127. [[CrossRef](#)]
9. Roberts, F.S.; Kuhl, K.P.; Nilsson, A. High selectivity for ethylene from carbon dioxide reduction over copper nanocube electrocatalysts. *Angew. Chem. Int. Ed.* **2015**, *127*, 5268–5271. [[CrossRef](#)]
10. Li, J.; Kuang, Y.; Meng, Y.; Tian, X.; Hung, W.H.; Zhang, X.; Li, A.; Xu, M.; Zhou, W.; Ku, C.S.; et al. Electroreduction of CO₂ to formate on a copper-based electrocatalyst at high pressures with high energy conversion efficiency. *J. Am. Chem. Soc.* **2020**, *142*, 7276–7282. [[CrossRef](#)]
11. Reddy, K.P.; Deshpande, P.A. Density functional theory study of the immobilization and hindered surface migration of Pt₃ and Pt₄ nanoclusters over defect-ridden graphene: Implications for heterogeneous catalysis. *ACS Appl. Nano Mater.* **2021**, *4*, 9068–9079. [[CrossRef](#)]
12. Li, Q.; Zhang, Y.; Shi, L.; Wu, M.; Ouyang, Y.; Wang, J. Dynamic structure change of Cu nanoparticles on carbon supports for CO₂ electro-reduction toward multicarbon products. *InfoMat* **2021**, *3*, 1285–1294. [[CrossRef](#)]

13. Shi, R.; Zhao, J.; Liu, S.; Sun, W.; Li, H.; Hao, P.; Li, Z.; Ren, J. Nitrogen-doped graphene supported copper catalysts for methanol oxidative carbonylation: Enhancement of catalytic activity and stability by nitrogen species. *Carbon* **2018**, *130*, 185–195. [[CrossRef](#)]
14. Carlsson, J.M.; Scheffler, M. Structural, electronic, and chemical properties of nanoporous carbon. *Phys. Rev. Lett.* **2006**, *96*, 046806. [[CrossRef](#)] [[PubMed](#)]
15. Wu, J.; Liu, M.; Sharma, P.P.; Yadav, R.M.; Ma, L.; Yang, Y.; Zou, X.; Zhou, X.D.; Vajtai, R.; Yakobson, B.I.; et al. Incorporation of nitrogen defects for efficient reduction of CO₂ via two-electron pathway on three-dimensional graphene foam. *Nano Lett.* **2016**, *16*, 466–470. [[CrossRef](#)]
16. Lim, D.H.; Jo, J.H.; Shin, D.Y.; Wilcox, J.; Ham, H.C.; Nam, S.W. Carbon dioxide conversion into hydrocarbon fuels on defective graphene-supported Cu nanoparticles from first principles. *Nanoscale* **2014**, *6*, 5087–5092. [[CrossRef](#)]
17. Liu, C.; He, H.; Zapol, P.; Curtiss, L.A. Computational studies of electrochemical CO₂ reduction on subnanometer transition metal clusters. *Phys. Chem. Chem. Phys.* **2014**, *16*, 26584–26599. [[CrossRef](#)]
18. Ma, Z.; Tsounis, C.; Kumar, P.V.; Han, Z.; Wong, R.J.; Toe, C.Y.; Zhou, S.; Bedford, N.M.; Thomsen, L.; Ng, Y.H.; et al. Enhanced Electrochemical CO₂ Reduction of Cu@Cu_xO Nanoparticles Decorated on 3D Vertical Graphene with Intrinsic sp³-type Defect. *Adv. Funct. Mater.* **2020**, *30*, 1910118. [[CrossRef](#)]
19. Hu, Q.; Han, Z.; Wang, X.; Li, G.; Wang, Z.; Huang, X.; Yang, H.; Ren, X.; Zhang, Q.; Liu, J.; et al. Facile synthesis of subnanometric copper clusters by double confinement enables selective reduction of carbon dioxide to methane. *J. Mater. Chem. A* **2020**, *59*, 19054–19059. [[CrossRef](#)]
20. Perez, G.; Marcandalli, G.; Figueiredo, M.C.; Calle, V.F.; Koper, M.T. Structure-and potential-dependent cation effects on CO reduction at copper single-crystal electrodes. *J. Am. Chem. Soc.* **2017**, *139*, 16412–16419. [[CrossRef](#)]
21. Liu, C.; Yang, B.; Tyo, E.; Seifert, S.; DeBartolo, J.; Zapol, P.; Vajda, S.; Curtiss, L.A. Carbon dioxide conversion to methanol over size-selected Cu₄ clusters at low pressures. *J. Am. Chem. Soc.* **2015**, *137*, 8676–8679. [[CrossRef](#)] [[PubMed](#)]
22. Yang, B.; Liu, C.; Halder, A.; Tyo, E.C.; Martinson, A.B.; Seifert, S.; Zapol, P.; Curtiss, L.A.; Vajda, S. Copper cluster size effect in methanol synthesis from CO₂. *J. Phys. Chem. C* **2017**, *121*, 10406–10412. [[CrossRef](#)]
23. Zhang, H.; Yang, Y.; Liang, Y.; Li, J.; Zhang, A.; Zheng, H.; Geng, Z.; Li, F.; Zeng, J. Molecular Stabilization of Sub-Nanometer Cu Clusters for Selective CO₂ Electromethanation. *ChemSusChem* **2022**, *15*, e202102010. [[CrossRef](#)] [[PubMed](#)]
24. Passalacqua, R.; Parathoner, S.; Centi, G.; Halder, A.; Tyo, E.C.; Yang, B.; Seifert, S.; Vajda, S. Electrochemical behaviour of naked sub-nanometre sized copper clusters and effect of CO₂. *Catal. Sci. Technol.* **2016**, *6*, 6977–6985. [[CrossRef](#)]
25. Wei, W.; Lu, Y.; Chen, W.; Chen, S. One-pot synthesis, photoluminescence, and electrocatalytic properties of subnanometer-sized copper clusters. *J. Am. Chem. Soc.* **2011**, *133*, 2060–2063. [[CrossRef](#)] [[PubMed](#)]
26. Schutz, M.; Muhr, M.; Freitag, K.; Gemel, C.; Kahlal, S.; Saillard, J.Y.; Da Silva, A.C.; Da Silva, J.L.; Fassler, T.F.; Fischer, R.A. Contrasting structure and bonding of a copper-rich and a zinc-rich intermetallic Cu/Zn cluster. *Inorg. Chem.* **2020**, *59*, 9077–9085. [[CrossRef](#)]
27. Su, X.; Jiang, Z.; Zhou, J.; Liu, H.; Zhou, D.; Shang, H.; Ni, X.; Peng, Z.; Yang, F.; Chen, W.; et al. Complementary Operando Spectroscopy identification of in-situ generated metastable charge-asymmetry Cu₂-CuN₃ clusters for CO₂ reduction to ethanol. *Nat. Commun.* **2022**, *13*, 1322. [[CrossRef](#)]
28. Uzunova, E.L.; Seriani, N.; Mikosch, H. CO₂ conversion to methanol on Cu(I) oxide nanolayers and clusters: An electronic structure insight into the reaction mechanism. *Phys. Chem. Chem. Phys.* **2015**, *17*, 11088–11094. [[CrossRef](#)]
29. Zhao, Z.; Peng, X.; Liu, X.; Sun, X.; Shi, J.; Han, L.; Li, G.; Luo, J. Efficient and stable electroreduction of CO₂ to CH₄ on CuS nanosheet arrays. *J. Mater. Chem. A* **2017**, *5*, 20239–20243. [[CrossRef](#)]
30. Lu, Y.F.; Dong, L.Z.; Liu, J.; Yang, R.X.; Liu, J.J.; Zhang, Y.; Zhang, L.; Wang, Y.R.; Li, S.L.; Lan, Y.Q. Predesign of Catalytically Active Sites via Stable Coordination Cluster Model System for Electroreduction of CO₂ to Ethylene. *Angew. Chem. Int. Ed.* **2021**, *60*, 26210–26217. [[CrossRef](#)]
31. Zhang, J.; Dai, L. Heteroatom-doped graphitic carbon catalysts for efficient electrocatalysis of oxygen reduction reaction. *ACS Catal.* **2015**, *5*, 7244–7253. [[CrossRef](#)]
32. Navalon, S.; Dhakshinamoorthy, A.; Alvaro, M.; Antonietti, M.; Garcia, H. Active sites on graphene-based materials as metal-free catalysts. *Chem. Soc. Rev.* **2017**, *46*, 4501–4529. [[CrossRef](#)] [[PubMed](#)]
33. Li, C.; Yuan, Y.; Hu, Y.; Zhang, J.; Tang, Y.; Ren, B. Density functional theory study of the structures and electronic properties of copper and sulfur doped copper clusters. *Comput. Theor. Chem.* **2016**, *1080*, 47–55. [[CrossRef](#)]
34. Zhang, Q.Y.; Zhao, Q.F.; Liang, X.M.; Wang, X.L.; Ma, F.X.; Suo, B.B.; Zou, W.L.; Han, H.X.; Song, Q.; Wu, Q.; et al. Computational studies of electrochemical CO₂ reduction on chalcogen doped Cu₄ cluster. *Int. J. Hydrogen Energy* **2018**, *43*, 9935–9942. [[CrossRef](#)]
35. Natesakhawat, S.; Lekse, J.W.; Baltrus, J.P.; Ohodnicki Jr, P.R.; Howard, B.H.; Deng, X.; Matranga, C. Active sites and structure-activity relationships of copper-based catalysts for carbon dioxide hydrogenation to methanol. *ACS Catal.* **2012**, *2*, 1667–1676. [[CrossRef](#)]
36. Carugno, S.; Chassaing, E.; Rosso, M.; Gonzalez, G.A. Enhanced electrochemical oxidation of methanol on copper electrodes modified by electrocorrosion and electrodeposition. *Mater. Chem. Phys.* **2014**, *143*, 1012–1017. [[CrossRef](#)]
37. Periasamy, A.P.; Liu, J.; Lin, H.M.; Chang, H.T. Synthesis of copper nanowire decorated reduced graphene oxide for electro-oxidation of methanol. *J. Mater. Chem. A* **2013**, *1*, 5973–5981. [[CrossRef](#)]
38. Peterson, A.A.; Abild Pedersen, F.; Studt, F.; Rossmeisl, J.; Norskov, J.K. How copper catalyzes the electroreduction of carbon dioxide into hydrocarbon fuels. *Energy Environ. Sci.* **2010**, *3*, 1311–1315. [[CrossRef](#)]

39. Zhang, J.; Dolg, M. ABCluster: The artificial bee colony algorithm for cluster global optimization. *Phys. Chem. Chem. Phys.* **2015**, *17*, 24173–24181. [[CrossRef](#)]
40. Hertwig, R.H.; Koch, W. On the parameterization of the local correlation functional. What is Becke-3-LYP? *Chem. Phys. Lett.* **1997**, *268*, 345–351. [[CrossRef](#)]
41. Rassolov, V.A.; Ratner, M.A.; Pople, J.A.; Redfern, P.C.; Curtiss, L.A. 6–31G* basis set for third-row atoms. *J. Comput. Chem.* **2001**, *22*, 976–984. [[CrossRef](#)]
42. Frisch, M.J.; Trucks, G.W.; Schlegel, H.B.; Scuseria, G.E.; Robb, M.A.; Cheeseman, J.R.; Scalmani, G.; Barone, V.; Petersson, G.A.; Nakatsuji, H.; et al. *Gaussian 16 Revision C.01*; Gaussian Inc.: Wallingford, CT, USA, 2016.
43. Neese, F.; Wennmo, F.; Hansen, A. Efficient and accurate local approximations to coupled-electron pair approaches: An attempt to revive the pair natural orbital method. *J. Chem. Phys.* **2009**, *130*, 114108. [[CrossRef](#)] [[PubMed](#)]
44. Kupka, T.; Stachów, M.; Nieradka, M.; Kaminsky, J.; Pluta, T.; Sauer, S.P. From CCSD(T)/aug-cc-pVTZ-J to CCSD(T) complete basis set limit isotropic nuclear magnetic shieldings via affordable DFT/CBS calculations. *Magn. Reson. Chem.* **2011**, *49*, 231–236. [[CrossRef](#)] [[PubMed](#)]
45. Neese, F. Software update: The ORCA program system, version 4.0. *Wiley Interdiscip. Rev. Comput. Mol. Sci.* **2018**, *8*, e1327. [[CrossRef](#)]
46. Takano, Y.; Houk, K. Benchmarking the conductor-like polarizable continuum model (CPCM) for aqueous solvation free energies of neutral and ionic organic molecules. *J. Chem. Theory Comput.* **2005**, *1*, 70–77. [[CrossRef](#)] [[PubMed](#)]
47. Kresse, G.; Joubert, D. From ultrasoft pseudopotentials to the projector augmented-wave method. *Phys. Rev. B* **1999**, *59*, 1758. [[CrossRef](#)]
48. Blochl, P.E. Projector augmented-wave method. *Phys. Rev. B* **1994**, *50*, 17953. [[CrossRef](#)]
49. Perdew, J.P.; Burke, K.; Ernzerhof, M. Generalized gradient approximation made simple. *Phys. Rev. Lett.* **1996**, *77*, 3865. [[CrossRef](#)]
50. Grimme, S. Semiempirical GGA-type density functional constructed with a long-range dispersion correction. *J. Comput. Chem.* **2006**, *27*, 1787–1799. [[CrossRef](#)]
51. Mathew, K.; Kolluru, V.S.C.; Hennig, R.G. VASPsol: Implicit Solvation and Electrolyte Model for Density-Functional Theory. 2018. Available online: <https://github.com/henniggroup/VASPsol> (accessed on 1 November 2021).
52. Norskov, J.K.; Rossmeisl, J.; Logadottir, A.; Lindqvist, L.; Kitchin, J.R.; Bligaard, T.; Jonsson, H. Origin of the overpotential for oxygen reduction at a fuel-cell cathode. *J. Phys. Chem. B* **2004**, *108*, 17886–17892. [[CrossRef](#)]
53. Zhang, J.; Glezakou, V.A.; Rousseau, R.; Nguyen, M.T. NWPEsSe: An adaptive-learning global optimization algorithm for nanosized cluster systems. *J. Chem. Theory Comput.* **2020**, *16*, 3947–3958. [[CrossRef](#)]
54. Malloum, A.; Fifen, J.J.; Conradie, J. Exploration of the potential energy surface of the ethanol hexamer. *J. Chem. Phys.* **2019**, *150*, 124308. [[CrossRef](#)]
55. Khan, M.A.; Wang, N.; Zhang, L.; Guo, X.; Huang, S. Analysis and assessment of the structural, electronic properties of (ZrH₂)_n (n = 5 – 24) clusters: Density function theory calculations. *Comput. Theor. Chem.* **2020**, *1188*, 112940. [[CrossRef](#)]
56. Malloum, A.; Conradie, J. Solvent effects on the structures of the neutral ammonia clusters. *Comput. Theor. Chem.* **2020**, *1191*, 113042. [[CrossRef](#)]
57. Malloum, A.; Fifen, J.J.; Conradie, J. Large-Sized Ammonia Clusters and Solvation Energies of the Proton in Ammonia. *J. Comput. Chem.* **2020**, *41*, 21–30. [[CrossRef](#)]